

Balmer- α and Balmer- β emission cross sections for H+Ar collisions

B. Van Zyl, H. Neumann, H. L. Rothwell, Jr., and R. C. Amme

Department of Physics, University of Denver, Denver, Colorado 80208

(Received 9 August 1979)

Absolute cross sections for the emission of Balmer- α and Balmer- β radiations from H+Ar collisions between about 25- and 2500-eV hydrogen-atom energy and the polarizations of the emitted radiations are reported. For hydrogen-atom energies above 250 eV, the contributions to these radiations from decay of the long-lived 3s and 4s excited states of hydrogen are resolved. The emission cross sections reach maximum values in the 100-eV hydrogen-atom energy range, where they are larger than the ionization cross sections for this reacting pair. The experimental techniques used to make the measurements are described and the results are compared with the work of other investigators. The available data are considered on the basis of a suggested model for the interaction.

I. INTRODUCTION

The Balmer-alpha (H_α) and Balmer-beta (H_β) emission lines of atomic hydrogen play important roles in many diverse areas of physics. From their fundamental contributions to the development of the Bohr model of the atom to their current importance in understanding hydrogen-containing plasmas, these emissions have served as valuable tools to the physicist and astronomer. Their emission wavelengths (at 656.28 and 486.13 nm, respectively) are easily observable, a fact which has enhanced their usefulness to the scientific investigator.

This paper reports measurements of the emission cross sections for these radiations for H+Ar collisions from 25- to 2500-eV hydrogen-atom energy. Our motivation for these studies stems from the need to interpret the observation of these emissions in the proton aurora,¹ where they are amongst the more prevalent atomic spectral features present under some conditions.² Since our measurements show that these emission cross sections have maxima in the 100-eV hydrogen-atom range and in fact are the largest inelastic cross sections yet measured in this low-energy region, the results presented should also be of interest to the basic understanding of such reaction types.

The accompanying paper³ presents the same emission cross sections for H^+ +Ar collisions over approximately the same energy range. The fact that these cross sections have energy dependencies vastly different from those reported here, and are considerably smaller in magnitude at their maxima, points to the significant differences between the details of the two interactions.

In addition to the difficulties associated with production of a low-energy neutral-hydrogen-atom beam of known intensity and the absolute calibration of the photon detector used, these

measurements must resolve a third problem relating to the long lifetimes of the 3s and 4s excited states of the hydrogen atom (1.6 and 2.3×10^{-7} sec, respectively). Thus, a hydrogen atom excited to one of these states in collision with an Ar target can travel many cm (at 10^7 – 10^8 cm/sec velocity) before decaying with the appropriate Balmer-line emission. The technique employed to overcome this difficulty is described in Sec. II, where the neutral-beam generation, target-density determination, and photon-detector-calibration procedures are also discussed. A bonus comes with solving this lifetime-related problem, however, in that the fractions of the H_α and H_β radiations which originate from these long-lived states can be separated from the total emission observed for H-atom energies above 250 eV.

The results of the radiation polarization and absolute cross-section measurements are presented in Sec. III. This section also includes a comparison of our results with data obtained by other investigators and a discussion of the results on the basis of the interaction of these colliding species.

II. EXPERIMENTAL PROCEDURE

A. Apparatus description

The technique used for generating the fast H-atom beam involves photodetaching electrons from negative hydrogen ions. The H^- ions, extracted from a duoplasmatron source, are mass analyzed and focused into a parallel or slightly convergent beam about 1 mm in diameter.⁴ This beam is then directed through the cavity of a yttrium aluminum garnet laser (1064 nm) modified to have totally reflecting end mirrors. The reaction



proceeds with an efficiency such that several percent of the H^- ions are neutralized at 500 eV.⁵

The details of the procedure are described elsewhere.⁶ The laser operates with a 50% duty-cycle square-wave time dependence, giving rise to a modulated H-atom flux with the same time dependence. This permits convenient separation of the photon-counting signal from background, as discussed below. The absolute flux of the H-atom beam ($\sim 10^{11}$ atoms/sec) is determined to within $\pm 3\%$ uncertainty down to 63-eV energy, increasing to about $\pm 12\%$ at 25 eV.

This energy-selected and highly collimated H-atom beam then enters the target scattering cell shown schematically in Fig. 1, through a 5-mm diameter differential-pumping aperture. During each cross-section measurement, the target pressure (typically $1-4 \times 10^{-4}$ Torr) is monitored with a Bayard-Alpert ionization gauge. Before and after such periods, the gauge is calibrated against a capacitance-diaphragm manometer, which is in turn calibrated in the 0.1-Torr region against an absolute micrometer-point contact oil manometer of the type described by Ruthberg.⁷ The capacitance-diaphragm manometer linearity between these pressure ranges has been demonstrated⁸ to be within $\pm 2.1\%$. Combining this uncertainty with others associated with the pressure and temperature measurements gives an absolute uncertainty of $\pm 6\%$ and a relative uncertainty (one target gas to another) of $\pm 4\%$ for the target-gas-density de-

termination.

The basic photon detector is also shown in Fig. 1. Photons produced by H+Ar collisions along the beam axis pass through the target-cell and vacuum-wall windows, are focused into a parallel beam by lens 1, pass through the appropriate interference filter, and are imaged onto the photocathode of a cooled photomultiplier tube (EMI 9658). The detector's viewing field is established by the square aperture (2 cm by 2 cm) inside the target cell and the circular apertures (4 cm diameter) fronting lenses 1 and 2. The focal lengths of lenses 1 and 2 are about 19 and 7.5 cm, respectively, giving rise to a 2.5 times demagnification of the scattering region at the photocathode. Note that the Polaroid plate can be inserted into the photon path as well to allow study of the polarization of the emitted light.

The interference filters are about 10^{-4} uv-to-ir-blocking types with maximum transmissions at line centers ranging from 42 to 71%. Their full width at half-maximum (FWHM) transmission band-passes are typically about 1 nm wide.

The entire photon detector and the square aperture inside the target cell can be moved along the H-atom beam axis to allow observation of photons from various positions along the axis, i.e., at various penetration depths into the cell. This feature allows a partial separation of radiations from the emitting states of the excited hydrogen atoms, as will be described below.

Figure 1 shows that an electron beam passes beneath the photon detector in a direction normal to the H-atom beam. This electron beam, which is modulated to the same time dependence as the H-atom beam, is included to calibrate the photon detector. The electrons are emitted from a tight-loop filament and accelerated towards a shaped anode for maximum current through the anode aperture. An Einzel lens then focuses the electrons through a 1-mm diameter aperture serving as a virtual cathode for a second such lens which focuses the electrons into an approximately parallel beam of about 4-mm diameter as it passes beneath the photon detector. The electrons then enter a guarded Faraday-cup collector where backscattered or secondary electrons are trapped. An electron energy of 500 eV is normally employed, the electron currents, on the order of $5 \mu\text{A}$, being determined to within $\pm 3\%$ uncertainty. To make certain that the same part of the photocathode receives light from either electron or H-atom impact collisions (appearing approximately as an 8-mm long "strip" of light at the photocathode surface), the entire photon detector is rotated through 90° when the electron beam is in use.

Great care was taken to assure the absence of

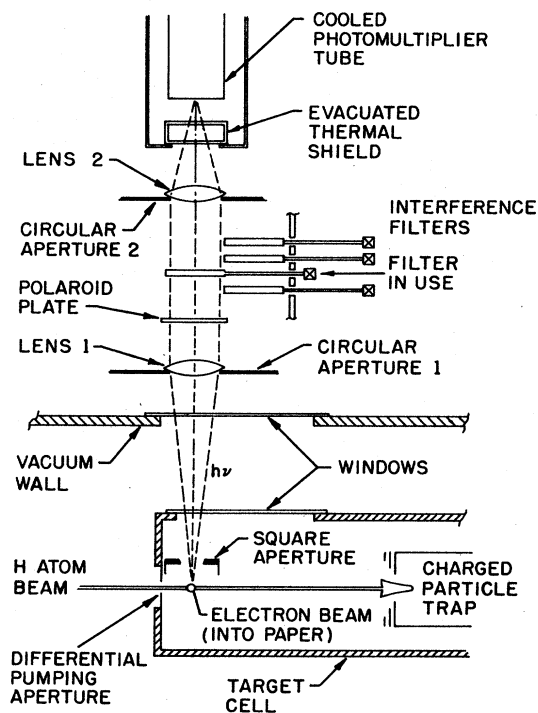


FIG. 1. The target cell and photon detector.

stray electric fields within the target cell to prevent Stark mixing of the various excited states of the hydrogen atom. In addition, a Helmholtz coil (and other magnetic shielding) was used to keep the magnetic fields in the interaction region below 0.1 G, so that the $\vec{v} \times \vec{B}$ electric fields in the fast H-atom reference frame were minimal.

Two counters, sharing an input from the photomultiplier pulse amplifier/discriminator, are gated on/off to receive counts during the beam on/off cycles (after small delays to avoid the switching intervals). Since all recognized sources of background counts were found to be dc in character, the difference between the registered counter outputs is thus a measure of the desired photon signal. The analog outputs of the ionization gauge supply and the instruments used to monitor the various beam intensities are integrated for present accumulation times (typically 40 sec) and recorded with the counter outputs for computer analysis. All recording channels are calibrated against standard current and voltage sources before and after each cross-section measurement period.

B. Background radiation check

Since the Ar atom has spectral lines in the vicinity of the H_α and H_β radiations of interest, it is necessary to show that such background emissions are not contributing substantially to the desired photon signal. This is accomplished by performing tilting interference filter (TIF) scans over the spectral regions of interest.

If λ_f is the wavelength at which an interference filter has maximum transmission for photons at normal incidence, the maximum transmission wavelength $\lambda_f(\phi)$ for other angles is given approximately by

$$\lambda_f(\phi) = \lambda_f \left[1 - \left(\frac{\sin \phi}{n} \right)^2 \right]^{1/2}, \quad (2)$$

where n is an "effective index of refraction" for the filter. Thus by starting with a filter whose λ_f is a few nm on the long wavelength side of the spectral line on interest, it is possible to scan the region around the line by angular rotation (tilting) of the filter in the light beam path.

For these studies, the interference filter station shown in Fig. 1 is replaced by a TIF assembly which allows the tilt angle to be set to within $\pm 0.1^\circ$. The result of such a test, a scan over the spectral region including H_α emission from H+Ar collisions at 500-eV H-atom energy, is shown in Fig. 2(a).⁹ Note that the curve shown has the shape of a typical filter transmission-versus-wavelength curve for about a 1-nm FWHM bandpass filter. Indeed, if no other radiations except a single spectral line

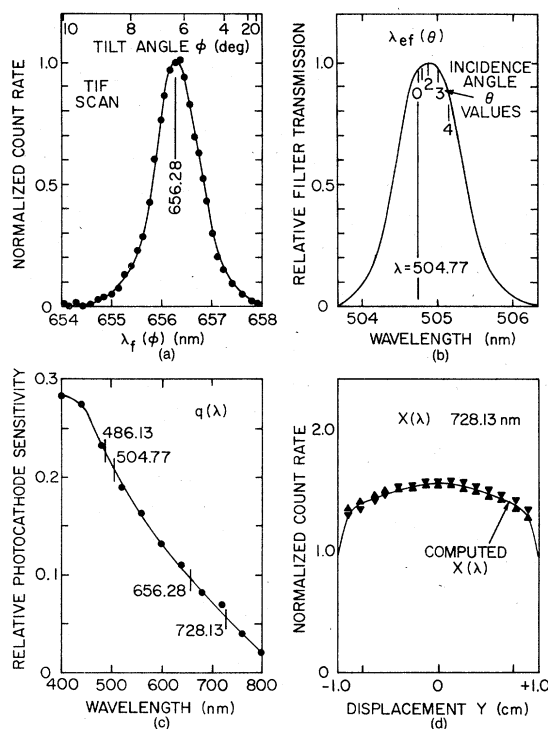


FIG. 2. (a) TIF wavelength scan over the H_α emission line. (b) Relative interference filter transmission versus photon angle of incidence. (c) Photomultiplier sensitivity versus wavelength. (d) Measured and computed variation of $X(\lambda)$ with coordinate y .

are present, such a scan should effectively mirror the filter transmission profile (except for a slight decrease in maximum transmission and increase in bandpass).¹⁰ If other emissions are present, one would expect a distorted or perhaps even double-peaked curve unless, of course, the other emission falls at the same wavelength as H_α (656.28 nm). No such emission is present in the Ar spectrum.

For the case of H_β radiation, two Ar spectral lines, at 486.22 and 485.94 nm, fall fairly close to the H_β wavelength (486.13 nm). The Ar atom transitions are $13s[1\frac{1}{2}]^0 - 4p[2\frac{1}{2}]^0$ and $3d[2\frac{1}{2}]^0 - 4s[1\frac{1}{2}]^0$, respectively.¹¹ The first of these requires outer-level electron excitation to quite a high quantum state and is therefore not likely to be an important contributor to the observed photon signal. No such argument, however, can be made for the second transition.

Nevertheless, we feel that it is highly unlikely that this Ar-atom radiation is contributing appreciably to the observed photon signal. First, the 485.94-nm Ar line is about 0.2 nm from H_β , and any substantial amount of radiation at this wavelength should distort the TIF scan to some extent.

No such distortion is found. Second, both of these Ar lines are only weakly observed in discharge spectra, orders of magnitude down in intensity from the brighter lines present.¹¹ Finally, the H $_{\beta}$ emission cross section reported here is large and exhibits an H-atom energy dependence very similar to that found for the H $_{\alpha}$ emission cross section, suggesting that similar processes are responsible for the observations. No correction (or increased uncertainty) has therefore been made to the data presented.

C. Photon-detector calibration

As noted earlier, an electron beam is included in the apparatus to allow absolute calibration of the photon detector. Since this is the first of a series of papers presenting H $_{\alpha}$ and H $_{\beta}$ emission cross sections for H and H $^{+}$ collisions with various target atoms and molecules, a fairly complete discussion of the detector calibration is given.

Absolute emission cross sections for the reactions



for $n=3-6$ decaying to the 2^1P level of He have recently been measured by Van Zyl *et al.*¹² Since the upper states from which radiation is observed are 1S in character, the radiation is unpolarized and isotropically emitted. In particular, the 3^1S-2^1P transition (at 728.13 nm) and the 4^1S-2^1P transition (at 504.77 nm) fall at wavelengths near the H $_{\alpha}$ and H $_{\beta}$ lines of interest here. For 500-eV electron impact, the emission cross sections are $9.23 (\pm 3.5\%) \times 10^{-20}$ and $2.05 (\pm 2.8\%) \times 10^{-20}$ cm 2 , respectively. These emission cross sections serve as the basis of our photon-detector-calibration procedure.

For an electron or H-atom beam passing through a low-density gas target, the total photon production rate per unit volume at wavelength λ is given by

$$\frac{dS(\lambda)}{dV} = F_b N_t \sigma(\lambda), \quad (4)$$

where F_b is the beam flux, N_t is the target density, and $\sigma(\lambda)$ is the emission cross section. If a coordinate system with x along the beam axis, y perpendicular to the axis, and z in the vertical direction of the photon detector is used, the observed photon counting rate will be

$$C(\lambda) = N_t \sigma(\lambda) \int F_b(y, z) E(x, y, z, \lambda, \lambda_f) dx dy dz, \quad (5)$$

where $E(x, y, z, \lambda, \lambda_f)$ is the total detector efficiency for photons emitted from point x, y, z and λ_f is the peak transmission wavelength (for normal incidence photons) of the interference filter used.

The spatial integral must be performed over the extent of the detector's viewing field.

The detector efficiency $E(x, y, z, \lambda, \lambda_f)$ is composed of the solid-angle acceptance of the optical system, the transmission of the optical components, the interference filter transmission, and the net quantum efficiency of the photomultiplier, i.e.,

$$E(x, y, z, \lambda, \lambda_f) = \left(\frac{\Omega(x, y, z)}{4\pi} \right) T_0(x, y, z, \lambda) \times T_f(x, y, z, \lambda, \lambda_f) Q_m(x, y, z, \lambda). \quad (6)$$

Fortunately, some simplification of this expression and thereby the integral of Eq. (5) is possible.

For the limited range of x, y, z covered in this experiment, the net transmission of the various windows and lenses is essentially independent of the point of photon origin. Thus, the approximation that $T_0(x, y, z, \lambda) \approx T_0(\lambda)$ is made and $T_0(\lambda)$ is in turn calculated from the indices of refraction for the materials used.

For the optical configuration used, the total detector efficiency should not exhibit a strong dependence on coordinate z for small z displacements from the electron or H-atom beam axis (i.e., the effect of beam diameter in this dimension should be small). This was verified by deflecting the electron beam in the $\pm z$ direction and noting that the measured photon counting rate was essentially unchanged. Thus, the dependence of the parameters in Eq. (6) on z can be dropped.

The solid angle $\Omega(x, y)$ can be computed with relative ease. Since the source of photons is located at the focal point of lens 1 (see Fig. 1), the photon trajectories beyond this lens are parallel, and the solid angle is given simply by the projected overlap of circular apertures 1 and 2. Even where the square aperture inside the target cell begins to restrict the solid angle, the calculations are not difficult.

The interference filter transmission $T_f(x, y, \lambda, \lambda_f)$ for a uniform filter located in the parallel light beam between lenses 1 and 2 should depend upon position x, y only from the fact that each x, y defines an angle θ at which photons are incident on the filter. If a photon of wavelength λ is incident on the filter at angle θ relative to the normal, the filter views this photon as having an effective wavelength $\lambda_{\text{ef}}(\theta)$ given by

$$\lambda_{\text{ef}}(\theta) = \lambda \left[1 - \left(\frac{\sin \theta}{n} \right)^2 \right]^{-1/2}, \quad (7)$$

where n is the effective index of refraction of the filter.¹³ For angles out to about 4° (the geometrical limit for our detector), λ_{ef} can be shifted by 0.3 to 0.4 nm from λ for the filters used. For

filters having FWHM transmission widths of only about 1.0 nm, the effects of such wavelength shifts can be substantial.

The data in Fig. 2(b) are presented as an example of how the filters were chosen. Shown is the relative filter transmission curve for the filter used to view the 504.77 nm radiation from $e^- + \text{He}$ collisions. The $\lambda_{\text{ef}}(\theta)$ positions for various θ are marked. Note that the relative transmission curve peaks at about 2° incidence angle. This constitutes an ideal situation, since the wavelength uncertainties (± 0.05 nm) associated with this transmission measurement¹³ and the filter temperature variations encountered from day to day ($\pm 1.5^\circ\text{C}$ with a filter temperature coefficient of about $0.013 \text{ nm}/^\circ\text{C}$) cause the wavelength scale to be uncertain by about 0.07 nm. Any such wavelength shifts thus increase the relative transmission for $\theta < 2^\circ$ and decrease the transmission for $\theta > 2^\circ$ (or vice versa) causing minimal change in the net relative transmission, which is obtained by integration along the beam path beneath the detector (and thus, over the angular range of θ covered).

Similar data were obtained for the other filters employed. It is estimated that the wavelength scale and temperature variation uncertainties should give rise to a net uncertainty of $\pm 2.5\%$ in the integrated relative filter transmission data for the 504.77-nm-line emission from He and for H_α emission from hydrogen. This uncertainty increased to $\pm 3.5\%$ for the H_β filter and to $\pm 4.5\%$ for the 728.13-nm He-line filter. (These uncertainties include the results of a study of the dependence of the relative filter transmissions on temperature between 18 and 26°C , normal operating temperature being $23.0 \pm 1.5^\circ\text{C}$.)

Assume for the moment that the net quantum efficiency of the photomultiplier is independent of the photon source position x, y and is given simply by

$$Q_m(x, y, \lambda) = \epsilon q(\lambda), \quad (8)$$

where $q(\lambda)$ is the relative photocathode sensitivity as a function of λ , and ϵ is a wavelength-independent efficiency parameter associated with the photomultiplier gain and the pulse-counting discriminator setting. The sensitivity $q(\lambda)$ was provided by the photomultiplier manufacturer (EMI) as a costed calibration service, and their data are shown in Fig. 2(c). The results are claimed to be accurate to within about $\pm 10\%$ on an absolute basis, but our needs call only for a relative $q(\lambda)$ versus wavelength, which is here estimated to be uncertain by $\pm 4\%$. The wavelengths of interest are marked on the curve shown.

Under the various approximations discussed

above, the observed photon-counting rate can be written as

$$C(\lambda) = \epsilon I_b N_f \sigma(\lambda) \left(\frac{\Omega_c}{4\pi} \right) T_o(\lambda) T_f(\lambda_f) q(\lambda) X(\lambda), \quad (9)$$

where $X(\lambda)$, the "effective beam path length viewed," contains those parameters requiring integration over the detector's viewing field; i.e.,

$$X(\lambda) = \iint \left(\frac{\gamma_b(y)}{I_b} \right) \left(\frac{\Omega(x, y)}{\Omega_c} \right) \times \left(\frac{T_f(x, y, \lambda, \lambda_f)}{T_f(\lambda_f)} \right) dx dy. \quad (10)$$

Note that I_b , the total beam intensity, Ω_c , the solid angle at the center of the detector's viewing field, and $T_f(\lambda_f)$, the absolute interference filter transmission at its peak transmission wavelength λ_f , appear in the numerator of Eq. (9) and the denominator of Eq. (10). Thus $X(\lambda)$ contains only an integral over the spatial dependencies of these parameters, where $\gamma_b(y)$, the one-dimensional beam-flux profile, satisfies the normalization

$$I_b = \int \gamma_b(y) dy. \quad (11)$$

Thus for a given beam profile $\gamma_b(y)$, the calculated $\Omega(x, y)$, and the $T_f(x, y, \lambda, \lambda_f)$ filter transmission data of the type shown in Fig. 2(b) can be used to compute an $X(\lambda)$ for each wavelength of interest.

By moving the photon detector along the H-atom beam axis relative to the fixed electron-beam axis, it is possible to study the dependence of $X(\lambda)$ on the y coordinate (and thus the beam diameter) for the electron beam. The computed variation of $X(\lambda)$ with such y displacements is shown by the solid line in Fig. 2(d), where a comparison with two sets of measured results (taken for the normal and 90° -rotated detector orientations) is made. The agreement is quite good, indicating that the dependence of $X(\lambda)$ on y is small out to ± 0.5 cm, and what dependence is present can be approximately calculated.

During such studies, the image of the emitting target-gas region sweeps across the photomultiplier cathode surface as the coordinate y is varied. Since the computed $X(\lambda)$ assumes that the photocathode sensitivity is independent of photon source position x, y , i.e., no term of the type $Q_m(x, y, \lambda)$ is included in the $X(\lambda)$ integral, the agreement between these calculated and measured results supports the "uniform photocathode" assumption of Eq. (8). Nevertheless, a $\pm 3\%$ uncertainty in $X(\lambda)$ is included to account for what nonuniformity may exist.

The absolute interference filter transmissions $T_f(\lambda_f)$ were measured three times (at two different

TABLE I. Dependence of the photon-detector calibration parameters on emission-line wavelength.

λ (nm)	$T_0(\lambda)$	$T_f(\lambda_f)$	$q(\lambda)$	$X(\lambda)$
728.13	$0.623 \pm 0.5\%$	$0.443 \pm 3.1\%$	$0.056 \pm 4.0\%$	$1.547 \pm 5.8\%$
504.77	$0.615 \pm 0.5\%$	$0.463 \pm 5.2\%$	$0.208 \pm 4.0\%$	$1.754 \pm 4.6\%$
656.28	$0.621 \pm 0.5\%$	$0.712 \pm 6.3\%$	$0.095 \pm 4.0\%$	$1.632 \pm 4.5\%$
486.13	$0.614 \pm 0.5\%$	$0.425 \pm 4.5\%$	$0.227 \pm 4.0\%$	$1.688 \pm 5.2\%$

laboratories¹⁴) during the course of these studies. The uncertainties in these transmission values are taken to be 1.5 times the spread of the individual measurements.

Values of the wavelength-dependent photon detector calibration parameters, i.e., the last four quantities in Eq. (9), are given in Table I.¹⁵ The uncertainties listed represent our best estimates of the quadrature-combined relative uncertainties (one wavelength relative to another) in all factors composing these parameters.

By using the values in Table I, the computed $\Omega_c/4\pi$ (which was 0.003 01), the known cross sections for emission of the 728.13- and 504.77-nm radiations from He, and measuring the normalized count rates $C(\lambda)/I_p N_t$ observed¹⁸ from electron bombardment of He, the efficiency parameter ϵ in Eq. (9) and its uncertainty can be determined. The values obtained are $0.245 \pm 10.2\%$ and $0.252 \pm 10.3\%$, respectively.¹⁷ The closeness of these values indicates that the wavelength dependencies of the various parameters entering the calculation have been properly accounted for. Furthermore, the value of about 0.25 is close to that expected based on the low photomultiplier voltage applied (1200 v) and the pulse-counting discriminator setting used.¹⁸

Since the electron and H-atom beam diameters are similar, the wavelength-independent value of ϵ determined above can be used in Eq. (9) to obtain the H_α and H_β emission cross sections for H+Ar

collisions.¹⁵ To check the detector calibration procedure further, however, these same emissions were observed from dissociative excitation of H_2 by electron impact. The cross sections obtained are compared with other recent data¹⁹ in Table II.^{20,21} Note that the agreement between all measurements is within mutual uncertainties, the present results falling 0.8% below (for H_α) and 2.0% above (for H_β) the averages of the other data listed.²² This is taken as further evidence that the wavelength dependencies of the various parameters entering the detector calibration have been properly determined.

D. Excited-state lifetime effects

Since the lifetimes of the 3s and 4s excited states of hydrogen are long, atoms excited to these states in collisions with Ar can travel considerable distances before decaying. Fig. 3(a) shows the calculated relative dependencies of the photon emission rates from the 3s, 3p, and 3d states of hydrogen as a function of distance into the target cell. These data, calculated from the expression

$$F_{3l} = 1 - \exp(-x/v\tau_{3l}), \quad (12)$$

where x is the distance into the cell, v the hydrogen atom velocity, and τ_{3l} the excited-state lifetimes, show F_{3l} , the fraction of equilibrium between photon emission and collisional excitation per unit path length under thin-target (single-collision) conditions, for 800-eV atoms moving through the cell. Here, the target-cell pressure was assumed to have a step-function onset at $x=0$, the point of entry into the cell.

Figure 3(b) shows the (normalized) count rate obtained as a function of x for the H_α signal under the same conditions. These measured results should fit the expression

$$C(x) = C_{3s} F_{3s} + C_{3p} F_{3p} + C_{3d} F_{3d}, \quad (13)$$

where C_{3l} are coefficients giving the fractions of the total H_α signal coming from decay of the 3l states. Since $F_{3p} \approx F_{3d} \approx 1.0$ for $x \geq 3$ cm into the cell, the data have been least-squares fit to the sum of a constant term ($C_{3p} + C_{3d}$) and a term with the x dependence of radiation from the 3s state.

TABLE II. Comparison of the Balmer-alpha and Balmer-beta emission cross sections from dissociative excitation of H_2 by 500-eV electrons.

Workers (Ref.)	Emission cross sections (10^{-20} cm ²)	
	Balmer-alpha	Balmer-beta
Vroom and deHeer (19a)	$31.2 \pm 12.0\%$	$4.87 \pm 7.0\%$
Khayrallah (19b)	$30.7 \pm 11.8\%$	$4.80 \pm 11.8\%$
Möhlmann <i>et al.</i> (19c)	$33.1 \pm 10.0\%$	$5.26 \pm 15.0\%$
Present results	$31.4 \pm 14.8\%$	$5.08 \pm 14.3\%$

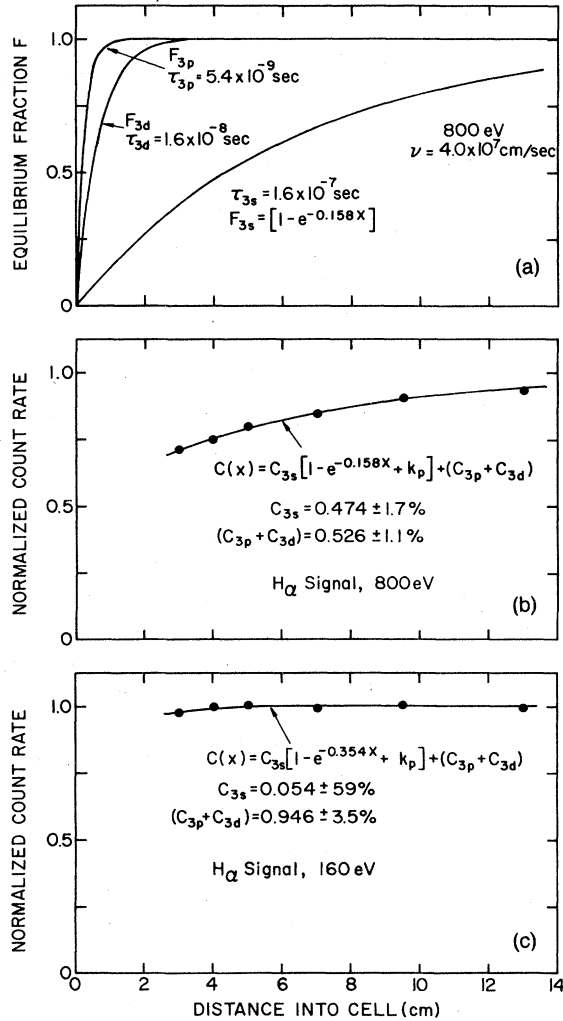


FIG. 3. (a) Computed target-cell equilibrium fractions for H_α emission from the $3s$, $3p$, and $3d$ states of hydrogen. (b) Measured H_α signal as a function of distance into the target cell at 800-eV H-atom energy. (c) Measured H_α signal as a function of distance into the target cell at 160-eV H-atom energy.

The uncertainties in the fit coefficients result from the fitting analysis. (The quantity K_p is a small correction applied to F_{3s} to account for the facts that the pressure profile near the cell entrance does not have a true step-function onset and that the pressure prior to the cell entrance is finite. The value of K_p , typically $1.0 \pm 0.5\%$ of F_{3s} , was computed from an estimated pressure profile near and prior to the cell entrance aperture.) By summing C_{3i} ($1.0 \pm 0.7\%$ for the normalized data shown), the total emission cross section can be obtained.

Data of the type shown in Fig. 3(b) were always taken as a function of target-cell pressure and the pressure-normalized count rates extrapolated to

zero pressure to remove the effects of second-collision processes. In general, the pressure-normalized count rates decreased with increasing pressure and with increasing distance into the target cell (where the longer path lengths through the cell afforded larger opportunity for multiple collisions). The magnitudes of the extrapolations required ranged from essentially zero for H-atom energies below 500 eV to about 10% at the highest energies and longest cell distances. This signal decrease was attributed to attenuation of the H-atom beam (conversion to protons via the ionization-stripping process, which have a much smaller H_α emission cross section³) and nonradiative collisional deactivation of the long-lived $3s$ -state hydrogen atoms in second collisions.

Since the ionization-stripping cross section for H+Ar collisions is known,²³ the amount of beam attenuation could be computed and was found to be only a few percent. If the remainder of the pressure-normalized signal decrease with increasing pressure is attributed to collisional deactivation of $3s$ -state excited atoms, the cross section for this process would have to be on the order of $2 \times 10^{-15} \text{ cm}^2$ in the 2-keV energy region. While highly uncertain, this value is in very rough agreement with the value of $3.1 \pm 1.0 \times 10^{-15} \text{ cm}^2$ obtained by Hughes and Kisner²⁴ for 10-keV H($3s$) atoms.

For H-atom energies below 250 eV , the separation of the radiation contributions from the $3p$ and $3d$ and the $3s$ states becomes more difficult. This is due to the fact that F_{3s} is closer to unity at these lower velocities. It seems clear, however, that most of the signal in the $100\text{--}250\text{-eV}$ energy region comes from decay of the short-lived $3p$ and $3d$ states. Data in this region are typified by the 160-eV results shown in Fig. 3(c).

For the case of H_β emission, the contributions from the $4s$, $4p$, and $4d$ states are more difficult to resolve. This comes about because the lifetime of the $4d$ state is $3.7 \times 10^{-8} \text{ sec}$ (about 2.3 times longer than for the $3d$ state), and the equilibrium fraction F_{4d} is still well below unity for the data taken near the cell front at the higher velocities. Thus, the fitting procedure used for the $n=3$ states was not applicable.

In principle, the result of Eq. (13) can be applied (for $n=4$) by setting $F_{4p} = 1$ (the $4p$ lifetime is still very short) and using the computed F_{4s} and F_{4d} to solve for the three C_{4i} coefficients. However, it was found that the data were simply not of sufficient quality to allow a meaningful three-parameter fit. In general, C_{4p} was found to be very small, but the fit gave negative values in some cases.

That C_{4p} was found to be small is not unreasonable since only about 12% of the hydrogen atoms

excited to this state will decay via H_β emission (the remainder decaying via Lyman-gamma and Paschen-alpha emission).²⁵ Thus, a fit of the form

$$C(x) = C_{4s}F_{4s} + (C_{4p} + C_{4d})F_{4d} \quad (14)$$

was used to reduce the data at the higher velocities. This led to results which were consistent with the simpler fit (where $F_{4d} \approx 1$) when applied to the data taken at large distances into the cell, but yielded much-reduced fitting uncertainties. An analysis revealed that so long as $C_{4p} \lesssim 0.5C_{4d}$ (which certainly seems to be the case here), the uncertainty involved in determining the total H_β emission cross section from this approximation did not exceed a few percent, even though the relative C_{4l} values might be uncertain by twice this amount. At the lower energies, of course, no such difficulty occurs since $F_{4d} \approx 1$ in this region.

E. Cascade effects

With one exception, the cascade contributions to the measured signals should not be large. This can be seen from the expressions (for the $n=3$ states)

$$S(3s) = P_{3s} + 0.038P_{4p} + 0.039P_{5p} + \dots, \quad (15)$$

$$S(3p) = 0.118(P_{3p} + 0.416P_{4s} + 0.319P_{5s} + \dots + 0.254P_{4d} + 0.236P_{5d} + \dots), \quad (16)$$

and

$$S(3d) = P_{3d} + 0.004P_{4p} + 0.004P_{5p} + \dots + P_{4f} + 0.637P_{5f} + \dots, \quad (17)$$

where $S(3l)$ are the signals resulting from the decay of the $3l$ states and P_{nl} are the probabilities for excitation to the various nl states.²⁵

Note that only small fractions ($\approx 4\%$) of the hydrogen atoms excited to the higher-lying np states decay to the $3s$ and $3d$ states (the np states decaying primarily via Lyman-line emissions). While larger fractions of the higher-lying ns and nd states decay to the $3p$ state, the net effect of these cascade transitions is still small since only 11.8% of the excited atoms in the $3p$ states decay by H_α emission (the remaining 88.2% decaying via Lyman-alpha emission). Thus the only substantial contributions to the observed H_α signal from cascade processes will be from sequences of the type $nf \rightarrow 3d \rightarrow 2p$, which dominate the decay schemes for the nf states.

Since the lifetimes of the nf states are fairly long (e.g., $\tau_{4f} = 7.3 \times 10^{-8}$ sec), the decay of the $3d$ states so populated will exhibit a target-cell position dependence. An attempt was thus made to analyze data of the type shown in Fig. 3(b) by in-

cluding the $4f \rightarrow 3d \rightarrow 2p$ transition (presumably the most important of such processes). It was found that any appreciable assumed population of the $4f$ state yielded a fit of diminished quality, since the "effective lifetime" of this process is still somewhat shorter than the lifetime of the $3s$ state. Note, however, that the effective lifetime of such processes can be extended by including decay of higher-lying nf states and allowing the $4f$ state itself to be populated in turn via cascade from higher ng states. Indeed, it appears mathematically possible to construct an ensemble of high n , high l states which have an effective lifetime comparable to that for decay of the $3s$ state. Similar arguments can be made relative to the $n=4$ level of excitation.

Nevertheless, we feel that the bulk of the radiation observed to come from decay of long-lived states must come from the $3s$ and $4s$ states. The high quality of the target-cell-position fits to the measured signals, the fact that the excitation cross sections appear to drop off rapidly with increasing quantum number n , and the results of the radiation-polarization studies all tend to support this contention.

III. RESULTS AND DISCUSSION

A. Emission-cross-section results

The H_α and H_β emission cross sections for H+Ar collisions are presented in Fig. 4, where they are plotted as a function of laboratory H-atom energy. Also shown are the fractions of the observed radiations from the long-lived $3s$ and $4s$ states of hydrogen and from the short-lived p and d states. The results have been corrected for the polariza-

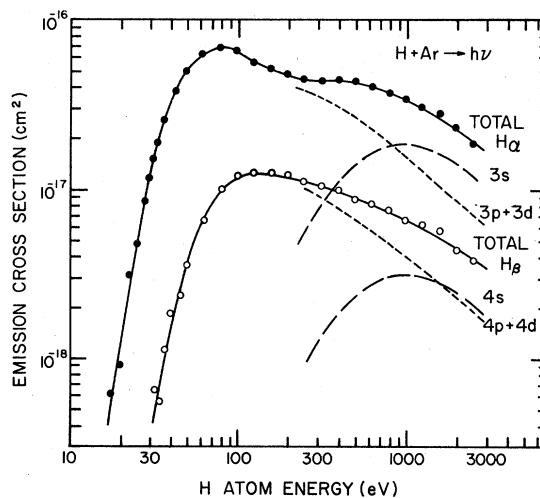


FIG. 4. H_α and H_β emission cross sections and individual state contributions.

tions of the emitted radiations.

The uncertainties in the total H_α emission cross section are $\pm 14\%$ down to an energy of 50 eV, increasing to $\pm 20\%$ at 25 eV, and to about $\pm 60\%$ at 17.5 eV. For the H_β results, the uncertainties are $\pm 16\%$ above 50 eV and increase to $\pm 30\%$ at 32 eV.

The uncertainties in the contributions to these cross sections made by the various individual states exhibit considerable variation. For example, at 800 eV, where the 3s and 3p+3d states contribute about equally to the H_α emission, the individual cross sections are uncertain by $\pm 15\%$ –17%, while at 250 eV, where the emission is dominated by decay of the 3p and 3d levels, their contribution is uncertain by only $\pm 14\%$. Here, however, the 3s state contribution is over $\pm 50\%$ uncertain. In general, where such individual contributions are large, their uncertainties are small, and vice versa.

The most striking features of these data are the large maxima in the emission cross sections in the 100-eV H-atom energy range. Furthermore, these maxima appear to be associated with emission from the short-lived excited states (probably from the 3d and 4d states, as will be argued later). Note that the H_α emission cross section is almost 10^{-16} cm² at only 80-eV H-atom energy and is still of order 10^{-18} cm² at only about 5 eV above the energetic threshold for the reaction (which is about 12 eV endothermic).

B. Radiation polarization results

As mentioned earlier, the polarization of the observed radiation (emitted at 90° to the H-atom beam axis) was measured in this experiment (see Fig. 1). In general, the polarization of such radiation, defined as

$$P = \frac{I_{\parallel} - I_{\perp}}{I_{\parallel} + I_{\perp}}, \quad (18)$$

where I_{\parallel} and I_{\perp} are the observed emission intensities with the planes of polarization parallel and perpendicular to the H-atom beam axis, can be used to obtain the total emission intensity from the relationship

$$I_{\text{total}} = I_{90^\circ} \frac{1}{3}(3 - P), \quad (19)$$

where I_{90° is the total intensity observed at 90° to the beam axis.

Actually, the situation is more complex in this experiment. The radiation from the 3s and 4s states should not be polarized.²⁶ Thus the directly measured polarizations were found to decrease with distance into the target cell, where decay from these levels represented a larger fraction of the observed light.

The procedure used to obtain a meaningful polarization measurement was thus to take data close to the cell entrance (at $x=3$ cm) where the contributions to the total radiation from the 3s and 4s states are smallest. After determining the fractions of the observed radiations coming from the *p* and *d* states in this position, the measured polarizations were corrected by division by these fractions to obtain the true polarizations of the radiations from these states. However, since at the lower energies only a total polarization could be determined (because the contributions from the long- and short-lived states could not be resolved), it was decided to present a total polarization at all energies. Thus the polarization of the light from the *p*+*d* states was reduced in accordance with the *s*-state radiation contributions at the higher energies.

The polarization results so obtained are shown in Fig. 5. Note that at the higher H-atom energies, where emissions from the 3s and 4s states dominate, the net polarizations are small, while at the lower energies the polarizations appear to be about 0.3. Such high values support the conclusion that most of the radiations in this low-energy region must come from the higher angular momentum states. The uncertainty flags shown in Fig. 5 represent both the statistical uncertainties of the directly measured polarizations and the uncertainties associated with the polarization-unfolding process described above, combined in quadrature.

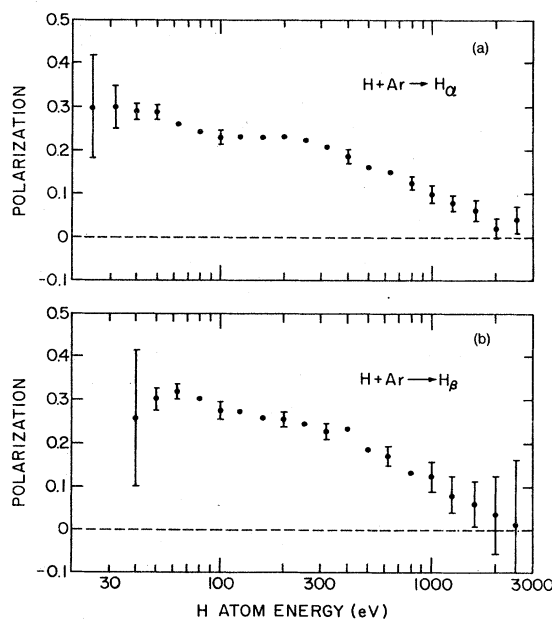


FIG. 5. Polarization of the total emitted H_α and H_β radiations.

C. Comparison with other excitation data

A comparison of the available data for excitation of hydrogen atoms to the $n=2$ and 3 levels for H+Ar collisions is made in Fig. 6. (Unfortunately, no other data are available at the $n=4$ level of excitation. The only other data of which we are aware are those for the Lyman-alpha emission cross section as reported by Dose *et al.*,³² which fall about a factor of 2.5 below the results shown between 2 and 50 keV H-atom energy.)

With the exception of the Lyman-alpha (L_α) emission cross sections shown in Fig. 6, all the other workers cited present "excitation" cross sections as opposed to "emission" cross sections (that is, the $3p$ -state excitation cross sections have been adjusted for the Lyman-beta/Balmer-alpha branching ratio for decay of this state.) While our lower-energy results have not separated the contributions to the observed H_α signal from the $3d$ and $3p$ states, and this excitation cross section can only be presented as that to the $3d$ state plus 12% of that to the $3p$ state, some such adjustments can be made for the $n=4$ level data to obtain the excitation cross sections. Thus the curve labeled $4s$ has been adjusted upward (from the emission data presented in Fig. 4) to

account for the Paschen-alpha decay route available to this state. A similar upward adjustment has been made to the curve labeled $4d + (\sim 0.12)4p$, but by assuming (for determining the adjustment factor) that all the radiation comes from decay of the $4d$ state. Hence this curve represents the $4d$ -state excitation cross section plus only approximately 12% of the $4p$ -state excitation cross section. Note, however, that these adjustments result in excitation cross sections which are systematically about a factor of 3.5 lower at the $n=4$ level than at the $n=3$ level for all the states involved.

If our $3d + (0.12)3p$ excitation cross section were to be attributed entirely to the 12% of the decay of the $3p$ state which results in H_α emission, the actual $3p$ -state excitation cross section would have to be about an order of magnitude above that reported by Orbeli *et al.*²⁸ in the few-keV H-atom energy range, and well above the L_α emission cross section at 1-keV H-atom energy. We do not feel that this is a likely situation, and therefore conclude that the bulk of the observed H_α emission from this hybrid excitation cross section must come from the $3d$ -state excitation.

There does not appear to be any violent disagreement between our $3s$ - and (basically) $3d$ -state ex-

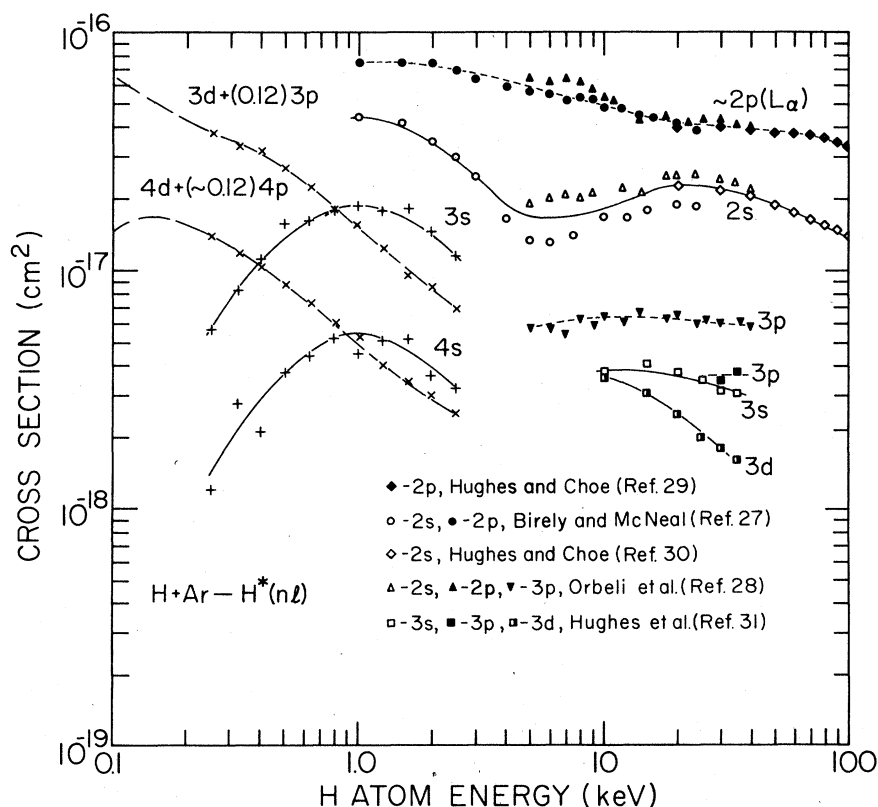


FIG. 6. Comparison of the present low-energy excitation cross sections with other higher-energy data for H+Ar collisions.

citation cross sections and those determined by Hughes *et al.*³¹ at the higher H-atom energies. On the other hand, it seems probable that these higher-energy cross sections are somewhat too small, because these workers did not account for possible collisional deactivation of excited hydrogen atoms in their (high pressure) target cell. This judgment is not inconsistent with the fact that the $3p$ -state excitation cross section determined by Orbeli *et al.*²⁸ (who made the measurement by observing Lyman-beta radiation) is above that reported by Hughes *et al.*³¹ (A similar situation is found for $H+N_2$ collisions, where more results are available for comparison.)

The large $3s$, $3d$, $4s$, and $4d$ excitation cross sections found here, which states must all make a cascade contribution to the population of the $2p$ state and thus show up in the L_α cross section measurements, suggest that the $2p$ -state population is heavily influenced by such cascade transitions. Indeed, at 1-keV H-atom energy, about one-half the L_α emission cross section reported by Birely and McNeal²⁷ can be accounted for by such cascade processes. (Actually, the situation may not be quite so bad, because many of the long-lived $3s$ - and $4s$ -excited atoms probably escape detection in the Birely and McNeal experiment. Thus their L_α cross-section measurements are

probably too small.)

In more serious doubt, however, are the $2s$ -state excitation cross sections reported by Birely and McNeal.²⁷ These measurements were made by noting the increase in their observed L_α signal when the radiation was observed from a region within the target cell where an electric field could be applied. While such a field will Stark-mix the $2p$ and $2s$ states, causing the $2s$ state to decay via L_α emission as well, the applied field will also mix the $3s$, $3p$; $4s$, $4p$; $3d$, $3p$; etc. states, opening the opportunity for decay of these higher-lying states via Lyman-beta, Lyman-gamma, etc. transitions during the "field-on" measurements. Thus the large cascade contribution for population of the $2p$ state will be substantially reduced in such a measurement, causing the $2s$ -state excitation cross section to be badly underestimated. Note that an upward shift of the $2s$ -state excitation cross section would appear to "scale" better with the value of the principal quantum number n .

D. Discussion of the H + Ar interaction

In a previous paper,²³ we reported cross sections for the reactions $H+Ar \rightarrow H+Ar^+ + e^-$, $H^+ + e^- + Ar$, and $H^- + Ar^+$ over approximately the same energy range covered in this experiment. Based on these results, we speculated that the $H^- + Ar^+$ Coulomb

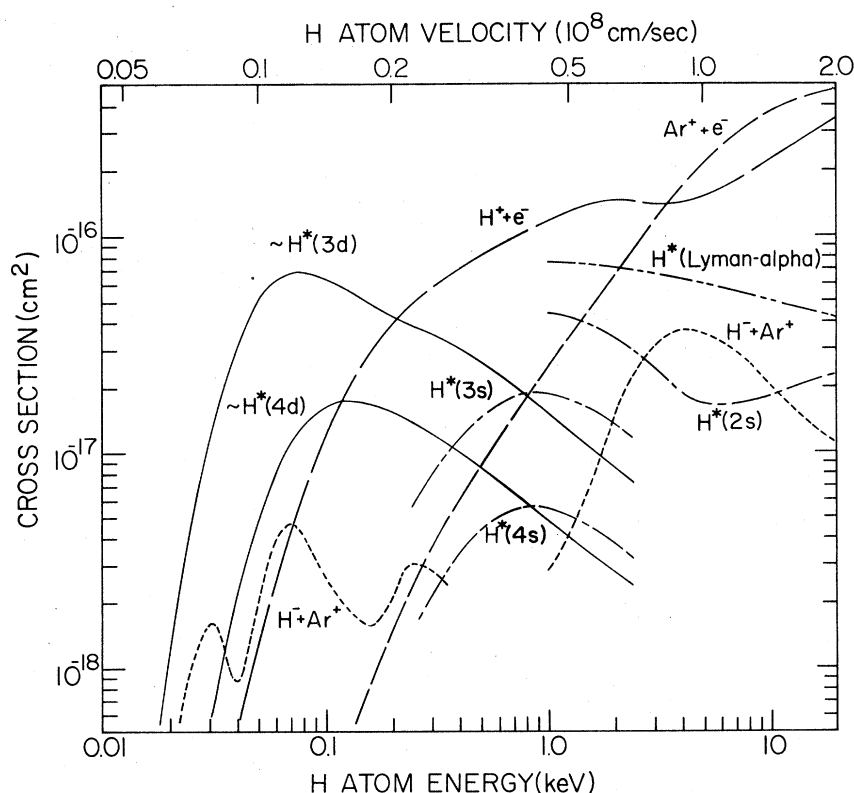


FIG. 7. Excitation and ionization cross sections for $H+Ar$ collisions. See text for the sources of the data presented.

state of the ArH molecule might serve as an "intermediate collision complex" which could explain the observations. The data upon which this speculation was based are shown in Fig. 7, where the present results and other recent data have also been included.

The $H^+ + e^-$ cross section data are from our results²³ (below 3 keV) and from Stier and Barnett³³ (above 4 keV). The $Ar^+ + e^-$ data include our results²³ (below 3 keV) and those of McNeal *et al.*³⁴ (above 3 keV). The $H^- + Ar^+$ results are from Aberle *et al.*³⁵ (below 100 eV), our work²³ (between 50 eV and 3 keV), and Stier and Barnett³³ (above 4 keV). The L_α emission and H(2s) excitation cross sections are again those of Birely and McNeal.²⁷ The present data for excitation of the 3s, 3d, 4s, and 4d states of hydrogen are also shown.

The reactions leading to the final-state collision products shown are all exothermic by more than 10 eV. Classically, one might expect the cross sections for such reactions to reach maxima at H-atom energies well above 10 keV. Yet, with the exception of the $Ar^+ + e^-$ cross section, all the other data exhibit maxima (or at least cross section structure) in the region below a few keV. Note in particular that the $H^- + Ar^+$ formation cross section drops very rapidly with decreasing energy in the 1–3-keV energy region ($v_H \approx 10^8$ cm/sec), in which region all the other cross sections (again excepting the $Ar^+ + e^-$ result) seem to be increasing or at least showing structure with decreasing energy.

Our interpretation of these data was based on a simple diabatic potential energy diagram of the type shown in Fig. 8(a). We postulated that the hydrogen and argon atoms came together along the ground-state H+Ar curve shown and made a transition to the $H^- + Ar^+$ state³⁶ at a crossing or near crossing of these curves somewhere inside ~ 1 Å internuclear separation. On the outward leg of the collision, however, this state could not survive its crossings with the states leading to H^* , Ar^* , and $H^+ + e^-$ (at least not for $v_H \approx 10^8$ cm/sec or so) and would thus "feed" these various collision-product channels. Of course, since the $H^- + Ar^+$ state does not cross the $Ar^+ + e^-$ state, this state could not be populated by this mechanism, giving rise to the structureless decrease with energy of this cross section.

Recently, the (adiabatic) potential-energy curves for many of the low-lying excited states of the ArH molecule have been calculated. Some of these are shown in Fig. 8(b). The X, A, B, and C curves for ArH and the $X(^1\Sigma)$ curve for ArH^+ are from Olson and Liu.³⁷ The D, E, F, and G curves (which lead to Ar^* at large separations) are from Vance and Gallup³⁸ (who also calculated the X, A,

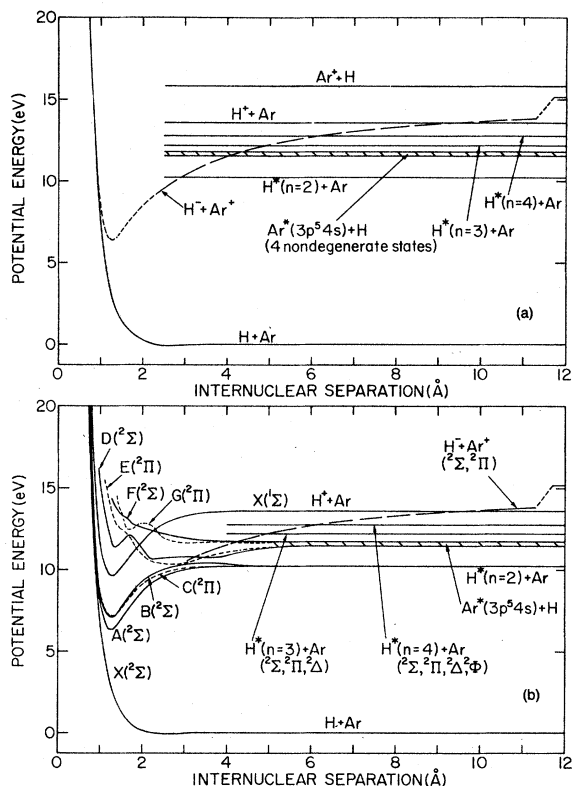


FIG. 8. (a) Diabatic and (b) adiabatic potential energy curves for the ArH molecule.

B, and C-state curves, but probably not as accurately as Olson and Liu). While no calculations of the $2^2\Sigma$, $2^2\Pi$, and $2^2\Delta$ curves which lead to the $n=3$ states of the hydrogen atom have been made, these curves, like the A, B, and C states must be Rydberg states of the ArH^+ ion as well. Thus, the D, E, F, and G curves calculated by Vance and Gallup (who did not include states leading to the $n=3$ level of hydrogen in their basis set) are too high in the region inside a few-Å separation, since these states will be "forced down" (by avoided crossings) by the $2^2\Sigma$ and $2^2\Pi$ states leading to the $n=3$ states of hydrogen.³⁹ It thus appears that there must be a multitude of states "packed" into the energy gap between the $B(^2\Sigma)$ state of ArH and the $X(^1\Sigma)$ state of ArH^+ .

The (diabatic) potential-energy curve for the $H^- + Ar^+$ state³⁶ from Fig. 8(a) has also been drawn in Fig. 8(b). Note that this curve (shown as a single curve but actually consisting of $2^2\Sigma$ and $2^2\Pi$ states) appears to merge towards the region occupied by the $A(^2\Sigma)$ state of ArH at the smaller separations. That this $A(^2\Sigma)$ state is rather "ionic" in character, can be nicely seen from the calculations of Vance and Gallup, who express the wave function for this state in terms of a linear combination of the wave

functions for the various states of the system at infinite separation, each being multiplied by the appropriate state-weighting coefficient. The coefficient multiplying the $H^- + Ar^+$ state becomes the largest term in the expansion for internuclear separations less than about 2 Å. Olson and Liu have also noted the importance of this Coulomb state by calculating the $A(^2\Sigma)$ well parameters with and without including this state in their basis set. They find that omission of this state gives a well depth for the $A(^2\Sigma)$ state of ArH which is substantially too small and not in good agreement with spectroscopic data.⁴⁰

The influence of the Coulomb state can be seen on other ArH states as well. For example, Vance and Gallup find that the $B(^2\Sigma)$ state is highly ionic in character in the internuclear separation region between about 2.5 and 3.5 Å [where this state appears to cross the diabatic $H^- + Ar^+$ state in Fig. 8(b)]. Similarly, the $D(^2\Sigma)$ state becomes ionic between 3 and 4 Å. Note also the (adiabatically) avoided crossing between these B and D states at about 3.5-Å separation, the downward trend in the B -state curve in this region probably reflecting its ionic nature. A similar situation results between the C and E states, again probably as a result of the influence of the $^2\Pi$ Coulomb state. Thus the effect of the Coulomb state can be followed right on through the calculated sequence of ArH molecular states, and there is little reason to doubt that similar avoided crossings would be found in the regions where the Coulomb-state energy and the energies of the $n=3$ and 4 levels of hydrogen are comparable.

Thus, whether we think of our collision model diabatically [with transitions at curve crossings as in Fig. 8(a)] or adiabatically [with transitions at avoided crossings as in Fig. 8(b)], the outcome is the same. That is, the reaction may proceed via a basically ionic intermediate molecular complex.

In Sec. III C above, it was argued that the large H_α and H_β emission cross sections reported here in the low-energy region most likely result from the decay of the $3d$ and $4d$ states of hydrogen. Furthermore, these radiations were found to be

highly positively polarized (see Fig. 5). With the help of Macek,⁴¹ we have calculated that the radiation from the $m_l=0, \pm 1$, and ± 2 magnetic substates of the $3d$ or $4d$ states should have polarizations of +0.48, +0.26, and -0.70, respectively. Since our measured polarizations are about +0.3 in the low-energy region, it would appear that the vast bulk of the observed emissions from the $3d$ and $4d$ states must come from the $m_l=0$ and ± 1 substates.

If the reaction process leading to these d -state-excited hydrogen atoms occurs on the outward leg of the collision and proceeds through a basically $H^- + Ar^+$ intermediate collision complex as postulated, the polarization data can be explained. In this picture, the $m_l=0$ substate would have to be correlated with a $^2\Sigma$ state of the ArH molecule. Similar correlations between the $m_l=\pm 1$ and ± 2 with $^2\Pi$ and $^2\Delta$ states, respectively, can be made. However, the (ground electronic) $H^- + Ar^+$ states can be only $^2\Sigma$ and $^2\Pi$ in character since the $Ar^+(^2P)$ and $H^-(^1S)$ states cannot be combined into a $^2\Delta$ configuration. Thus, the radiation-polarization data are certainly consistent with the proposed reaction model.

In summary, it appears that a class of (essentially chemical) inelastic reactions occur in low-energy H+Ar collisions. The available cross-section data for both ionization and excitation processes and the polarization of the light emitted following such collisions are consistent with (but do not prove) a reaction model involving the existence of an intermediate collision complex which is ionic in character.

ACKNOWLEDGMENTS

The authors express their thanks to R. E. Olson and J. H. Macek for helpful discussions, to J. R. Olson and B. Peterson for assistance in apparatus modification and maintenance, and to E. Barr and J. Noxon for interference filter characterization. This work has been supported by the Aeronomy Program, Division of Atmospheric Sciences, National Science Foundation.

¹Hydrogen atoms are important in the proton aurora because the incoming protons are largely converted to neutral atoms via charge transfer processes.

²See, for example, A. Omholt, *The Optical Aurora*, edited by J. G. Roederer and J. Zähringer (Springer-Verlag, Berlin, 1971).

³B. Van Zyl, H. L. Rothwell, Jr., and H. Neumann, following paper, *Phys. Rev. A* **21**, 730 (1980).

⁴Space charge causes the beam to spread to 3–4-mm

diameter below 100-eV energy.

⁵In general, the photodetachment efficiency has an inverse velocity dependence.

⁶B. Van Zyl, N. G. Utterback, and R. C. Amme, *Rev. Sci. Instrum.* **47**, 814 (1976).

⁷S. Ruthberg, *J. Vac. Sci. Technol.* **6**, 401 (1969).

⁸B. Van Zyl, *Rev. Sci. Instrum.* **47**, 1214 (1976).

⁹Such tests were performed at H-atom energies of 100, 500, and 2500 eV.

- ¹⁰R. H. Eather and D. L. Reasoner, *Appl. Opt.* **8**, 227 (1969).
- ¹¹A. R. Striganov and N. S. Sventitskii, *Tables of Spectral Lines of Neutral and Ionized Atoms* (IFI/Plenum, New York, 1968).
- ¹²B. Van Zyl, G. H. Dunn, D. W. O. Heddle, and G. E. Chamberlain (unpublished).
- ¹³Detailed studies of the interference filter properties including absolute transmission, transmission wavelength profile, wavelength shift with incident photon angle, and uniformity of transmission over the surface (with an absolute wavelength accurate to ± 0.05 nm) were performed at Barr Associates, West Concord, Mass.
- ¹⁴In addition to the studies at Barr Associates (see Ref. 13), the transmissions were measured at the Fritz Peak Observatory of National Oceanic and Atmospheric Administration, Boulder, Colorado.
- ¹⁵Various beam diameters and profiles, $\gamma_b(y)$, were used to calculate $X(\lambda)$. For diameters between 0 and 8 mm, the results were rather insensitive to diameter or profile. Appropriate uncertainties (typically $\pm 2\%$) have been included in $X(\lambda)$.
- ¹⁶The pressure-normalized counting rates $C(\lambda)/N_t$ were found to be functions of pressure in the amounts of $1.6 \pm 0.6\%/10^{-4}$ and $0.6 \pm 0.6\%/10^{-4}$ Torr at 728.13 and 504.77 nm, respectively. Appropriate extrapolations (and uncertainty increases) to zero pressure were made. This effect was attributed to radiation trapping in the higher n^1P states of He, which contribute to the observed emissions via cascade processes. See Ref. 12 for additional discussion of this effect.
- ¹⁷Values of ϵ were determined twice daily, both before and after each H_α and H_β cross section measurement run. The values quoted are averages over the course of the measurements.
- ¹⁸The settings were chosen to optimize the signal to dark count sensitivity ratio.
- ¹⁹(a) D. A. Vroom and F. J. de Heer, *J. Chem. Phys.* **50**, 580 (1969); (b) G. A. Khayrallah, *Phys. Rev. A* **13**, 1989 (1976); (c) G. R. Möhlmann, F. J. de Heer, and J. Loos, *Chem. Phys.* **25**, 103 (1977).
- ²⁰Our emission cross sections were not corrected for radiation polarization which is small at 500 eV (see Ref. 19). It was also assumed that molecular H_2 emissions were not being observed. [Ref. 19(b) describes work with similar interference filters and estimates such contributions should be less than 2%.] Finally, no correction was made for the fact that some 3s and 4s excited hydrogen atoms (which have ~ 0.2 μ sec lifetimes and up to about 7-eV energy from the dissociation process) may escape the detector's viewing field before radiating. Since our viewing field is large and only about 20% of the observed emissions come from these states [G. A. Khayrallah and S. J. Smith, *Chem. Phys. Lett.* **48**, 289 (1977), and included references], the fraction of the emission lost should not exceed about 2%. (Note that these last two problems may approximately negate one another in any case.) Appropriate uncertainties for these claims have been included.
- ²¹Our cross section values are averages of two determinations made about three months apart. The scatter in the values was only $\pm 1.1\%$ for H_α and $\pm 0.8\%$ for H_β .
- ²²An alternate calibration procedure would have been to use the averages of these other cross sections to determine ϵ , giving values of $0.240 \pm 15.5\%$ and $0.250 \pm 15.2\%$ at H_α and H_β , respectively (very close to the values of 0.245 and 0.252 found from He-atom excitation).
- ²³B. Van Zyl, T. Q. Le, H. Neumann, and R. C. Amme, *Phys. Rev. A* **15**, 1871 (1977).
- ²⁴R. H. Hughes and H. Kisner, *Phys. Rev. A* **5**, 2107 (1972).
- ²⁵Branching ratios were taken from E. U. Condon and G. H. Shortley, *The Theory of Atomic Spectra* (Cambridge University, Cambridge, England, 1963).
- ²⁶Since the 3s- and 4s-state wave functions are spherically symmetric, there can be no preferred orientation for their emission pattern.
- ²⁷J. H. Birely and R. J. McNeal, *Phys. Rev. A* **5**, 257 (1972).
- ²⁸A. L. Orbeli, E. P. Andreev, V. A. Ankudinov, and V. M. Dukelskii, *Sov. Phys. JETP* **30**, 63 (1970).
- ²⁹R. H. Hughes and S. S. Choe, *Phys. Rev. A* **5**, 656 (1972).
- ³⁰R. H. Hughes and S. S. Choe, *Phys. Rev. A* **5**, 1758 (1972).
- ³¹R. H. Hughes, H. M. Petefish, and H. Kisner, *Phys. Rev. A* **5**, 2103 (1972).
- ³²V. Dose, R. Gunz, and V. Meyer, *Helv. Phys. Acta.* **41**, 264 (1968).
- ³³P. M. Stier and C. F. Barnett, *Phys. Rev.* **103**, 896 (1956).
- ³⁴R. J. McNeal, D. C. Clark, and R. A. Klingberg, *Phys. Rev. A* **2**, 131 (1970).
- ³⁵W. Aberle, B. Brehm, and J. Grosser, *Chem. Phys. Lett.* **55**, 71 (1978).
- ³⁶The $H^- + Ar^+$ curve shown is simply the point-charge Coulomb potential energy down to about 2- \AA internuclear separation. The well shape inside this separation is only a crude estimate based on the shape of other such ionic curves.
- ³⁷R. E. Olson and B. Liu (private communication).
- ³⁸R. L. Vance and G. A. Gallup, *J. Chem. Phys.* (to be published).
- ³⁹The goal of the Vance and Gallup work (Ref. 38) was to determine the shapes of the A-G curves at separations larger than about 2 \AA .
- ⁴⁰R. E. Olson (private communication).
- ⁴¹J. H. Macek (private communication). The determinations were made by the procedures described in U. Fano and J. H. Macek, *Rev. Mod. Phys.* **45**, 553 (1973).